Gyrokinetic simulations of ion and impurity transport

C. Estrada-Mila, J. Candy, and R. E. Waltz

View Online   **Export Citation**

ARTICLES YOU MAY BE INTERESTED IN

AVS Quantum Science

Co-Published by

RECEIVE THE LATEST UPDATES

Gyrokinetic simulations of ion and impurity transport

C. Estrada-Mila
Department of Mechanical and Aerospace Engineering, University of California, San Diego, La Jolla, California 92093

J. Candy and R. E. Waltz
General Atomics, San Diego, California 92121

A systematic study of turbulent particle and energy transport in both pure and multicomponent plasmas is presented. In this study, gyrokinetic results from the GYRO code [J. Candy and R. E. Waltz, J. Comput. Phys. **186**, 545 (2003)] are supplemented with those from the GLF23 [R. E. Waltz, G. M. Staebler, W. Dorland *et al.*, Phys. Plasmas **4**, 2482 (1997)] transport model, as well as from quasilinear theory. Various results are obtained. The production of a particle pinch driven by temperature gradients (a thermal pinch) is demonstrated, and further shown to be weakened by finite electron collisionality. Helium transport and the effects of helium density gradient and concentration in a deuterium plasma are examined. Interestingly, it is found that the simple D-v (diffusion versus convective velocity) model of impurity flow is consistent with results obtained from nonlinear gyrokinetic simulations. Also studied is the transport in a 50-50 deuterium-tritium plasma, where a symmetry breaking is observed indicating the potential for fuel separation in a burning plasma. Quasilinear theory together with linear simulations shows that the symmetry breaking which enhances the tritium confinement arises largely from finite-Larmor-radius effects. To justify the numerical methods used in the paper, a variety of linear benchmarks and nonlinear grid refinement studies are detailed. © *2005 American Institute of Physics.* [DOI: 10.1063/1.1848544]

I. INTRODUCTION AND SUMMARY

Historically, gyrokinetic (GK) simulations have focused almost exclusively on the energy transport of core ions with little attention given to the study of plasma flow. However, several critical issues such as the existence of turbulent particle pinches in pure (one ion species) and impure (more than one ion species) plasmas, or the design and operation of the fueling and pumping systems for future burning plasmas, depend strongly on particle dynamics. For example, the projected performance of the International Thermonuclear Experimental Reactor (ITER) depends strongly on the fraction of accumulated helium ash during long-pulse or steady-state operation.[1] Similarly, the accumulation of impurities (injected or originating from material surfaces) in the core of a burning plasma can result in excessive fuel dilution or core radiation.

In this paper we present a detailed gyrokinetic study of ion particle and impurity transport. Full nonlinear gyrokinetic dynamics of all ions and electrons, trapped and passing, is simulated using the GYRO code[2] in the $\rho_* \to 0$ flux-tube (local) limit, where periodic boundary conditions and no profile variation are implied. We consider only electrostatic fluctuations relevant for low β and circular geometry. Although previous simulations have used this degree of realism, particle transport was not studied *per se*.[3–5] Earlier works on particle dynamics, focused on impurities in a tokamak[6,7] where impurity-driven instabilities and their effect on ion temperature gradient (ITG) modes were studied. However, these studies did not include trapped particles, the electron response was assumed to be adiabatic, and there was little or no discussion of impurity flows.

For the purposes of benchmarking and validation, we compare with linear simulations from both the GS2 code[8,9] and a second linear gyrokinetic code.[7] For nonlinear comparisons we use the reduced gyrofluid transport model GLF23.[10] We remark that the GLF23 model is based on fits derived solely from linear gyrokinetic and nonlinear gyro-Landau-fluid simulations (and more recently, GYRO gyrokinetic simulations). The methodology employed in this report was to initially find interesting qualitative characteristics of the transport using GLF23, and subsequently analyze them in more detail using the quantitative realism of GYRO.

The remainder of this paper is organized as follows: In Sec. II, a description of units and conventions used by the codes is presented. Section III shows linear benchmarks of GYRO with other GK codes and previous results in impurity transport. In Sec. IV an introduction to the nonlinear simulations is presented. This section consists of four separate parts. The first part introduces the simulation parameters used, followed by a discussion of resolution, code convergence, and the definition of quasilinear approximation used in this work. Section V studies pure plasmas and looks at the effect of temperature gradients, electron collisions, and curvature. Section VI looks at helium flow in deuterium plasmas; in particular, the effects of impurity density gradient and dilution on particle and energy transport are considered. This part also includes a critical review of multiple-species transport models currently in use. In Sec. VII we focus on the dynamics of a 50-50 deuterium-tritium (D-T) plasma. Here, we discover a robust flow separation effect which favors the improved confinement of tritium. In Sec. VIII, an analytical treatment, based on quasilinear theory, is used to

$$\chi_{\text{eff}} = \frac{n_i\chi_i + n_I\chi_I}{n_i + n_I}, \quad Q_{\text{eff}} = -(n_i + n_I)\chi_{\text{eff}}\frac{\partial T_i}{\partial r}. \quad (3)$$

In the previous expressions, r is a flux-surface label (physically, the midplane minor radius). All subsequent discussions and analysis are restricted to circular geometry and electrostatic fluctuations. We assume the usual definition of magnetic shear $s=(r/q)(dq/dr)$, where q is the safety factor.

TABLE I. Units and associated normalizations for results in this paper.

Dimension	Unit	Description
Length	a	Minor radius
Mass	m_i	Ion mass
Velocity	c_s	Ion sound speed $\sqrt{T_e/m_i}$

gain insight into the most interesting numerical results of the paper. Section IX gives a concluding summary.

II. UNITS AND CONVENTIONS

A. Basic units

Unless otherwise specified, the following conventions and units are employed throughout this paper. The choice of basic units is summarized in Table I. Frequencies and growth rates are normalized to c_s/a where $c_s \doteq \sqrt{T_e/m_i}$ is the ion sound speed, a is the plasma minor radius, and i is the main ion species. Because diffusivities have a natural gyro-Bohm scaling, we will generally normalize these to a reference gyro-Bohm level $\chi_{\text{GB}} \doteq \rho_s^2 c_s/a$, where $\rho_s \doteq c_s/\Omega_{ci}$ is the ion-sound Larmor radius and $\Omega_{ci} = z_i eB/m_i$ is the ion cyclotron frequency. In particular, for nonlinear studies, to avoid ambiguity we define a reference *deuterium* gyro-Bohm diffusivity χ_{GBD} for which $m_i \rightarrow m_D$. In this paper, the symbol σ is the most general species label for which three general values are allowed: i (main ion), I (impurity ion), and e (electron). Specific ion species present in the simulations will be denoted by their standard chemical symbol.

B. Fluxes and diffusivities

In the units described above, the particle and energy fluxes, Γ_σ and Q_σ, are related to the particle and energy diffusivities, D_σ and χ_σ, according to

$$\Gamma_\sigma = -D_\sigma\frac{\partial n_\sigma}{\partial r}, \quad Q_\sigma = -n_\sigma\chi_\sigma\frac{\partial T_\sigma}{\partial r}. \quad (1)$$

Γ_σ and Q_σ are computed as the magnetic flux surface, time, and radial averages of the primitive fluxes computed from the gyrokinetic equations. Converting quantities back to physical units is straightforward; for example, the physical radius is $a \times r$, the physical flux is $c_s \times \Gamma_\sigma$, and the physical diffusivity is $c_s \times a \times D_\sigma$. Density and temperature are in physical units.

We must warn the reader that in experimental work, the particle diffusivity is often separated into a diffusive part and a convective part

$$\Gamma_\sigma \rightarrow -D_\sigma^d\frac{\partial n_\sigma}{\partial r} - n_\sigma v_{\text{in}}, \quad (2)$$

where D_σ^d is the turbulent diffusion coefficient and v_{in} is an inward convective velocity. When inward convection dominates diffusion, there is a net inward flow of particles; we call this a particle pinch. For the analysis which follows, it will be convenient to define an effective ion energy diffusivity and effective ion flux as

C. Gradient scale lengths

The density and temperature gradient scale lengths are $L_{n\sigma} \doteq -[\partial(\ln n_\sigma)/\partial r]^{-1}$ and $L_{T\sigma} \doteq -[\partial(\ln T_\sigma)/\partial r]^{-1}$, respectively. Consequently, a negative density gradient means that particle density increases with radius (outwardly peaked profile), whereas a positive density gradient implies the usual inward-peaked profile.

For impurity studies the charge *dilution* is defined as $f_I \doteq z_I(n_I/n_e)$ where, as we have previously indicated, the subscript I refers to the impurity species. In order to satisfy plasma neutrality the following relation between density gradients must be satisfied:

$$\frac{1}{L_{ni}} = \frac{1/L_{ne} - f_I/L_{nI}}{1 - f_I}. \quad (4)$$

III. LINEAR BENCHMARKS

To validate the gyrokinetic impurity treatment in GYRO, we compared with independent linear runs of the GS2 code. At the level of this comparison, GYRO and GS2 are solving exactly the same equation (the gyrokinetic equation) and should in principle agree to desired accuracy. In order to make a connection with the existing literature, the parameters for the cross-code comparison were based on published work by Dong and Horton.[7] For this benchmark, hydrogen is the main ion and fully stripped carbon ($z_C=6$) is the impurity, electrons are taken to be adiabatic, and particle trapping is ignored. Although the parameter set employed here follows that of Ref. 7, the GYRO and GS2 calculations are done at finite aspect ratio ($R=3$ and $r=0.5$) and therefore include the dynamics of trapped ions.

First, in Fig. 1(a), we plot the growth rate as function of $k_\theta\rho_s$. Fixed parameters for this scan were $q=2.5$, $s=0.5$, $f_C = z_C(n_C/n_e)=0.5$, $f_i=n_i/n_e=0.5$, $L_{ne}=0.9$, $L_{nC}=-0.45$, $L_{ni}=0.225$, and $L_T=0.1125$. Figure 1(b), next, shows the effect of carbon concentration f_C. Fixed parameters in this case were $k_\theta\rho_s=1/\sqrt{2}$, $q=2.5$, $s=1$, $L_{ne}=0.9$, and $L_{nC}=-0.45$ with L_{ni} computed from Eq. (4) and $\eta_i=L_{ni}/L_T=2$.

We note excellent agreement between GYRO and GS2, indicating that both codes are functioning correctly. We have verified that the discrepancy in comparing with Ref. 7 cannot be fully attributed to finite-aspect-ratio effects, although the agreement with respect to growth rate does improve somewhat in the limit $r/R \ll 1$.
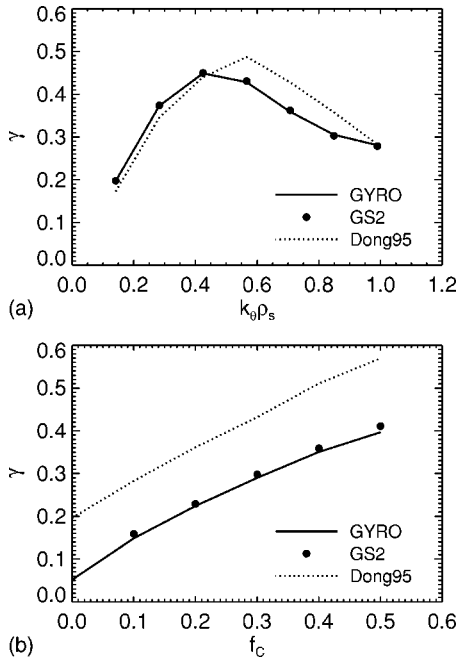
FIG. 1. Adiabatic electron comparison of growth rates for the GYRO (solid line) and GS2 (black dot) codes. Also shown are published results by Dong (Ref. 7) (dotted line) which neglect trapping. Plot (a) shows the growth rate as functions of $k_\theta \rho_s$. Plot (b) shows the effect of carbon concentration, $f_C \doteq z_C n_C/n_e$, for $k_\theta \rho_s = 1/\sqrt{2}$ and $s=1$. All other parameters are the same in both plots. Agreement between GYRO and GS2 is extremely good.

IV. NONLINEAR SIMULATIONS, METHODS, AND MODELS

The methodology employed here was to first find the qualitative behavior of selected cases using GLF23, and subsequently get quantitative results using GYRO. The salient point is that for the cases considered in this paper, a single GLF23 run takes less than a second on a desktop workstation, whereas GYRO takes about 5 h using 32 MSPs on the Cray X1. As mentioned in the Introduction, full gyrokinetic dynamics of all ion and electron species is included in the GYRO simulations. For most of the cases considered, the GYRO-GLF23 agreement is quite good, although in a minority of cases we have been able to find notable discrepancies. The scans in this paper were generated by varying four separate parameters: the impurity density gradient $1/L_{nI}$, the impurity dilution f_I, the ion and electron temperature gradients $1/L_T$ (simultaneously), and the electron-ion collision frequency ν_e. Plasma neutrality, which is reflected by the equality in Eq. (4), is always enforced.

A. Choice of equilibrium parameters

All nonlinear results use the *Standard Case* parameters[10] (for which GLF23 has been calibrated) as a reference point. These are $1/L_{Te}=1/L_{Ti}=3$, $1/L_{ne}=1/L_{ni}=1$, $R=3$, $r=0.5$, $s=1$, $q=2$, $T_e=T_i$, $\alpha=0$, $\beta_e=0$, $\nu_{ei}=0$, and $k_\theta \rho_s=0.3$. Deuterium is taken as the main ion species. In addition, we use kinetic electrons ($m_i/m_e \simeq 3600$) and simplified s-α circular geometry. All departures from this set of parameters will be explicitly indicated. Our motivation for using these parameters is twofold: (1) they are roughly typical of a central

location in the tokamak where the gyrokinetic equations are believed to provide an accurate description of the plasma, and (2) various previous studies have been done using them.

B. Code resolution

For the cases considered herein, we are interested in local studies only and thus run GYRO in the flux-tube limit. Our normal code resolution uses a 128-point velocity-space grid (eight energies, eight pitch angles, and two signs of velocity) and ten poloidal (orbit) grid points per sign of velocity. Experience gained over three years of GYRO use, after hundreds of simulations, indicates that ITG modes are in fact very well resolved at this velocity-space resolution even for non adiabatic electrons. Adequate resolution of the perpendicular directions $(x,y) \rightarrow (r,\varphi)$ tends to be more problematic and needs to be scrutinized for each parameter set. Since we are restricting attention to flux tubes, we content ourselves with an $(L_x,L_y)=(128,128)$ box, $n_r=140$ radial grid points (so that $\Delta r/\rho_s=0.91$), and $n_n=16$ complex toroidal modes. With these choices, we resolve up to $k_\theta \rho_s = 0.75$.

C. Convergence and adequacy of grid

Unpublished results by Hallatschek and Dorland[11] appear to suggest that simulations relevant to particle transport need to resolve very small radial and poloidal scales. The possibility of this effect motivated a perpendicular resolution study. For this we performed two runs using the resolution defined in the preceding section, but in a smaller $(L_x,L_y)=(64,64)$ box. The first used the same perpendicular grid size: $k_\theta \rho_s \lesssim 0.75$ and $\Delta r/\rho_s=0.91$ (achieved by setting $n_n=8$ and $n_r=70$). The second used twice the resolution in each dimension: $k_\theta \rho_s \lesssim 1.5$ and $\Delta r/\rho_s=0.46$ (obtained by taking $n_n=16$ and $n_r=140$). The results of these two small-box cases are compared with our baseline $(L_x,L_y)=(128,128)$ case, as summarized in Table II. Two conclusions are readily apparent. First, the smaller boxes slightly underestimate the transport magnitude in all channels. Indeed, Fig. 2 shows that the large box (dashed curve) is large enough to resolve the peak in the transport spectrum at $k_\theta \rho_s \sim 0.1$, whereas the small box (solid curve) does not resolve this peak and underestimates the transport by roughly 21%. Second, working at finer grid resolution (S/F versus S/C in Table II) reduces the outward particle and energy flows slightly. This may be due to a reduction of effective numerical (upwind) diffusion in the radial direction. The overall effect is insignificant. Note that Fig. 2 also shows that while the linear growth rate (dotted curve) in the trapped electron mode (TEM) regime is much higher than in the ITG regime, the actual TEM-driven transport is very small.

D. Quasilinear estimates

As an aid in understanding certain fully nonlinear results, we sometimes use a simple type of *quasilinear* approximation. This is nothing more than evaluating the nonlinear fluxes using the complex linear eigenmodes and eigenfrequencies at a selected $k_\theta \rho_s$. Specifically, the particle

TABLE II. Results for box-size and perpendicular-grid-size convergence study. In the "simulation" column, L=large box, S=small box; C=coarse grid, and F=fine grid. The L/C simulation is the base Standard Case. The L/C-to-S/C comparison demonstrates that a small 64×64 box slightly underestimates the transport. This result is well known to us from previous studies. The S/C-to-S/F comparison indicates that the coarse grid only slightly overestimates outward transport (probably a consequence of larger upwind dissipation in the coarse-grid case) but captures the essential physics.

Simulation	χ_i	χ_e	D_i	Δ_r/ρ_s	$(k_\theta\rho_s)_{\max}$	(L_x, L_y)
L/C	11.82	3.48	−1.93	0.91	0.75	(128,128)
S/C	9.33	2.76	−1.52	0.91	0.75	(64,64)
S/F	9.07	2.53	−1.62	0.46	1.5	(64,64)

flow is the product of the density perturbation $\tilde{n}$ and the perturbation of of the $E \times B$ velocity ($\tilde{v}_{E\times B}$) such that $\Gamma = \tilde{n}\tilde{v}_{E\times B}$. The quasilinear approximation takes $\tilde{n}_k = F(\omega_k) \times (\tilde{v}_{E\times B})_k$ for each mode k with F a complex linear function given by the linear response of the density perturbation to the potential perturbation at the complex linear mode frequency $\omega = \omega_R + i\gamma$.

V. PARTICLE TRANSPORT IN A PURE PLASMA

Before treating multiple ion species, we consider particle transport in a pure plasma. In particular, we would like to know when anomalous pinches (flow against density gradients) occur. This problem has perhaps been one of the most studied in particle transport, both theoretically and experimentally; in fact, such a pinch is necessary to explain observed equilibrium density profiles in the core of a tokamak, where the particle source is almost negligible and the plasma flow is virtually zero. Coppi and Spight[12] were the first to elaborate on a pinch theory, although their detailed arguments are more suitable for the edge of the plasma. Their proposed mechanism for inward flow is the so called *ion-mixing mode*, which includes the effect of ITG mode turbulence on the nonadiabatic electron response. It was argued that kinetic electrons determine the particle transport of ions and electrons (because transport is ambipolar). The analysis ignored toroidal and shear effects, and assumed the collisional drift wave (CDW) limit. Because of this last assumption, only the circulating electrons contribute to the pinch—
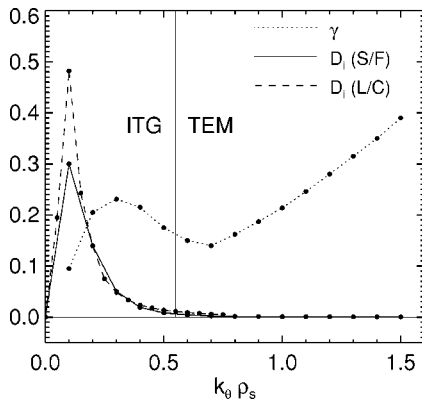

FIG. 2. Effect of high $k_\theta\rho_s$ on particle flow at two different resolutions: S/F and L/C (see Table II). Although for a TEM-dominated regime the growth rates are very high, the particle transport is close to zero.

specifically, a *thermal pinch* (also called *thermodiffusion*, as will be discussed shortly) since the inward flow component of the total transport is proportional to the temperature gradient, $1/L_{Te}$. The key insight of Coppi and Spight was to observe that at the null flow point where the density gradient outward drive is balanced by the inward temperature gradient drive, the CDW mode (which rotates in the electron direction) would be stable. Thus, an unstable ion-direction ITG mode is the required source of the turbulence. If the density peaks too much—driving η_i below threshold—the ITG mode will also be stabilized.

Subsequent works[13,14] attempted to generalize this paradigm to the more collisionless regime appropriate to the core. The details of the Coppi–Spight theory actually apply only to the highly collisional edge where the fueling supplies the flow and a pinch is usually not needed. Reference 13 considered the dissipative (low collisionality) regime where the trapped electron mode is excited and therefore can play a significant role. This study used sheared-slab geometry including an *ad hoc* division of electron velocity space into trapped and circulating regions. It was found that for the dissipative trapped electron mode (DTEM) the particle flow is outward. An improvement over this work[14] considered lower collisionality and showed that the trapped electron response can have a thermal pinch in the collisionless trapped electron mode (CTEM) regime. The major difference with previous works was that curvature was included, which allows a finite growth rate in the collisionless limit. It is worth mentioning that all the previous theories used quasilinear approximations to estimate the particle flow. More importantly, all of the acronyms used here (CDW, DTEM, and CTEM) in reality refer to the electron-direction drift wave in different collisionality regimes. In all cases the ion-direction ITG mode is required to drive the turbulence at the null flow point.

More recently, a new approach emerged where pinch effects are not directly associated with density or temperature gradients but involve magnetic field curvature which can induce a pinch as the result of subtle functional constraints.[15–18] Using a 3D fluid model of ITG/TEM turbulence, Garbet *et al.*[19] were able to confirm the existence of a curvature-drift pinch in addition to the usual thermal pinch.

A. Characteristics of a thermal pinch

Figure 3(a) shows the variation of the normalized ion thermal and particle diffusivities, χ_i and D_i, versus the nor-

(a)

(b)
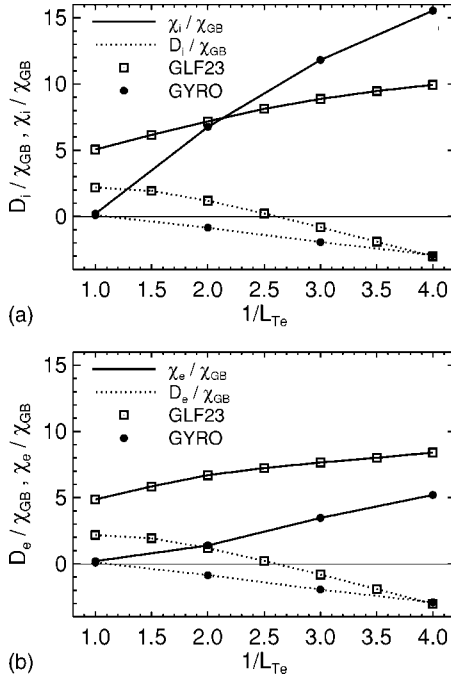
FIG. 3. L_{Te} scan (at fixed L_{ne}, with $L_{Te}=L_{Ti}$). Plot (a) compares the total ion particle (dotted line) and thermal (solid lines) diffusivity from GYRO (circles) to that from GLF23 (squares). In plot (b), a similar comparison is presented for the electron diffusivities.
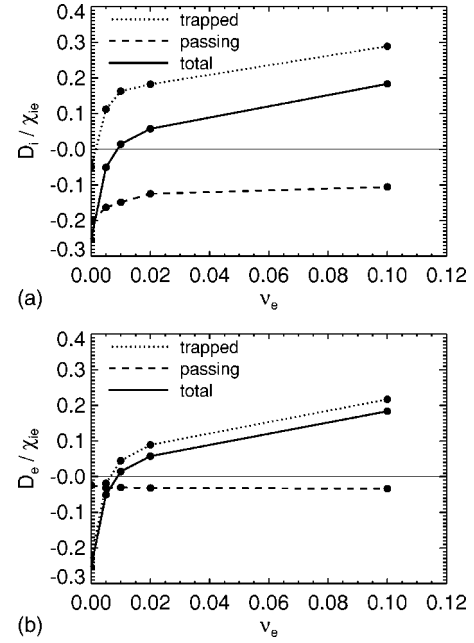

(a)

(b)

FIG. 4. Ion particle flow (a) and electron particle flow (b) separated into trapped and passing fractions. The flows are normalized to $\chi_{ie} \doteq (\chi_i+\chi_e)/2$.

malized temperature gradient for GLF23 and GYRO. In these simulations $L_{Te}=L_{Ti}$. Figure 3(b) shows the analogous plots for the electron dynamics. Both codes show a thermal pinch at sufficiently high η_e. However, GLF23 does not have an accurate threshold and the electron energy flow is too high.

B. Effect of electron collisions on a thermal pinch

It has been shown recently that—in the context of GLF23 transport modeling—electron collisions are needed to accurately reproduce the reduction of the anomalous particle pinch in ASDEX-U.[20] Looking again at the Standard Case in the collisionless limit, we observe a robust particle pinch (see Fig. 3 at $L_{ne}/L_{Te}=3$). However, Fig. 4 shows that this pinch is rapidly converted to outward particle flow as electron collisions are increased from zero. For higher collisionality, the trapped ions flow outward while the passing ions flow inward. This is quite in contrast to the relative behavior of the passing and trapped electron populations. Because the passing electrons are (nearly) adiabatic—and thus in phase with the potential—they suffer little transport. Therefore, to maintain charge neutrality, the trapped electrons must compensate and nearly balance the total ion particle flow. However, it is incorrect to conclude that the pinch disappears for higher collisionality. The pinch threshold simply moves to a higher η_e when collisionality is included.

VI. HELIUM TRANSPORT IN DEUTERIUM PLASMAS

A. Density gradient effects

We next consider the effect of density gradient scale length L_{nHe} on the particle transport for both ion species. It is of interest to determine when a turbulent pinch due to density gradient is created. In this section, the particle diffusivities D_{He} and D_i are normalized to the effective energy diffusivity χ_{eff} given by Eq. (3), whereas $1/L_{nHe}$ was normalized to $1/L_{ne}$. First, Fig. 5(a) shows the effect of helium density gradient (including negative, or inverted, gradients) on the D/χ ratio as estimated by the GLF23 code. Results are given for two impurity concentrations: $f_{He}=0.1$ and $f_{He}=0.3$. Figure 5(b) shows the GYRO simulations. The results are in very good qualitative agreement, showing that for sufficiently weak, positive helium gradient, a helium pinch is created. Figure 6 shows analogous plots for the main ions. For positive gradients, we see a robust inward flow of the main ions. This pinch feature of the Standard Case has been already noted in the preceding section for the case of a pure plasma. For $L_{nHe}/L_{ne}<0$ (helium peaked outside) the deuterium flow is outward and the helium flow is inward ($1/L_{ne}=1$ and $1/L_{nD}$ remains positive in these runs).

It is instructive to see in more detail how the value D_σ computed by GYRO is related to the diffusive and convective contributions to the transport. Eqs. (1) and (2) imply

$$D_{He} = D_{He}^d - v_{in}L_{nHe}. \tag{5}$$

If the D_{He}-L_{nHe} relationship is assumed to be linear (in other words, D_{He}^d and v_{in} are independent of L_{nHe}), then from Eq. (5) it follows that D_{He}^d is given by the vertical intercept in Fig. 7, whereas the convective velocity v_{in} is given by the slope. From this we can estimate an inward velocity of 12.4 and 11.6 (units of c_s) for $f_{He}=0.1$ and 0.3, respectively, and a turbulent diffusion coefficient $D_{He}^d/\chi_{GBD}=17$ for both dilu-
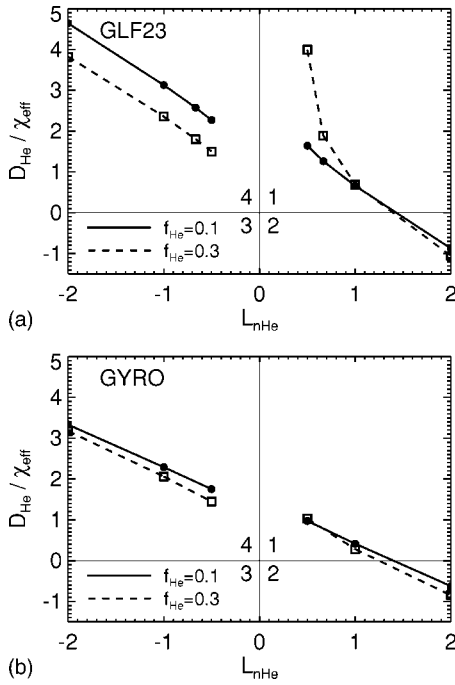
FIG. 5. Normalized impurity flow D_{He} vs L_{nHe} scan (at fixed $L_{ne}=1$) for two different impurity concentrations: $f_{He}=0.1$ and 0.3. Quadrant 1 refers to outward flow and a peaked profile, 2 to inward flow and peaked profile, 3 to outward flow and hollow profile, and 4 to inward flow and hollow profile. Plot (a) shows GLF23 results while plot (b) shows GYRO results.

FIG. 6. Same as Fig. 5, except showing the main ion flow D_i/χ_i rather than the impurity flow D_{He}/χ_i. As before, plot (a) shows GLF23 results while plot (b) shows GYRO results (both at fixed $L_{ne}=1$). According to Eq. (4), $1/L_{ni}>0$ in these scans.

tions. From this it seems that only convective processes have a dependence on impurity concentration, albeit a very weak one (compare solid and dashed lines in Fig. 7). Zero flux ($D_{He}=0$) necessarily implies a balance between convective and diffusive terms.

B. Dilution effects

The purpose of this section is to study the mechanics of (main ion) dilution and how all ion channels are affected by it. Two fundamental issues are discussed here: the first is the effect of f_{He} on particle transport; the second is the validity of conceivable approximations to multiple-species transport, such as the *dilution model* and the *lumped-mass approximation*. Neither of these discuss the transport of impurities and are intended only to describe the effect on energy transport. Here the dilution model is taken to mean that impurities do not respond to the potential and are assumed to have no flow. Equilibrium charge neutrality is maintained, so that the only effect of increasing f_{He} is the dilution of the main ions. The impurity ion gradient enters only via Eq. (4). The lumped-mass approximation, on the other hand, creates a *fictitious* species[6] with atomic mass M defined by

$$M = (1-f_I)m_i + f_I m_I. \tag{6}$$

For example, this would give rise, in a 50-50 D-T mixture, to the notion of a DT ion with an effective mass of $M=2.5 m_H$. If the impurity has a different charge state than the main ion, one might also introduce an effective charge
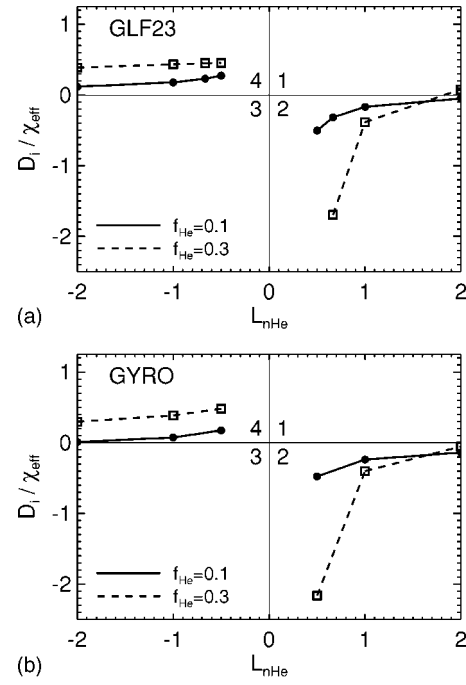
$$Z = (1-f_I)z_i + f_I z_I. \tag{7}$$

In this approximation, the lumped ion species is assumed to have the same profile as the background ions. For this study we have considered two qualitatively different plasmas: one in which impurities are inwardly peaked ($1/L_{nHe}>0$), such as helium ash born at the core, and the opposite case for which the impurities are outwardly peaked ($1/L_{nHe}<0$), such as incoming edge particles. For the lumped-mass approximation there is no distinction.

1. Inward impurity peaking

For positive $1/L_{nHe}$ there is little variation in the transport of helium [solid curves in Fig. 8(a)] as f_{He} is increased, whereas better deuterium confinement is predicted [solid
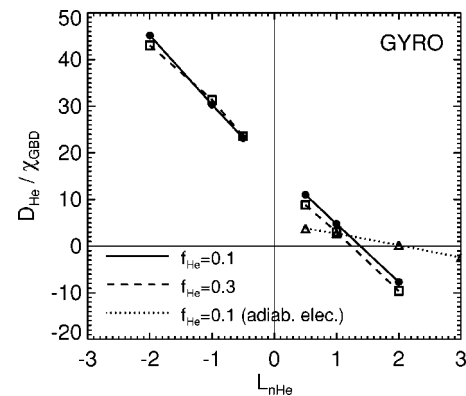

FIG. 7. Helium diffusivity D_{He} vs L_{nHe} scan (at fixed $L_{ne}=1$) for two different impurity concentrations: $f_{He}=0.1$ (solid line) and 0.3 (dashed line), using GYRO. The diffusive term D_σ^d is given by the vertical intercept of the graph whereas the convective velocity v_{in} is given by its slope. The dotted line shows the results for adiabatic electrons at $f_{He}=0.1$.
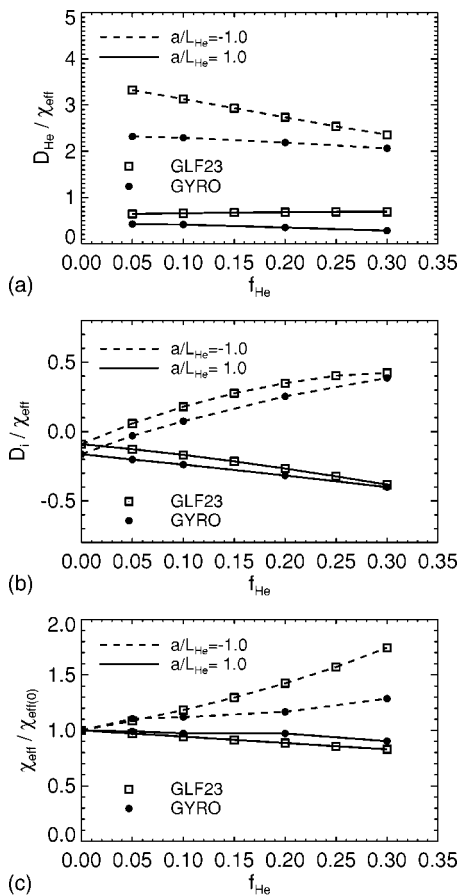
FIG. 8. Particle and heat flow, D_i, D_{He}, and χ_{eff} as functions of impurity fraction f_{He}. Here, two different impurity density gradients, $1/L_{nHe} = \pm 1$, are considered. Plot (a) compares D_{He} results for GLF23 and GYRO, plot (b) compares D_i results, and plot (c) compares effective heat diffusivity [normalized to $\chi_{eff}(0)$—the code-specific value at $f_{He}=0$].

curves in Fig. 8(b)]. This result agrees with experimental trends observed recently in DIII-D, and previously in several other machines (Ref. 21, and references therein). This corresponds to the so-called radiative impurity (RI) mode in which a controlled amount of impurities tends to improve confinement. For the case of energy transport, a similar trend is observed in Fig. 8(c) (solid line). The agreement between GYRO and GLF23 is impressive. Note that He is flowing out and D is flowing inward, and the electrons are pinched.

One of the key factors in a fusion plasma is the efficient removal of helium ash. Although this problem is global in nature, since ash is generated at the core and pumped out at the edge, we can use some of our results to address this problem. The most critical quantity in this problem is the ratio between the helium ash removal time and the energy confinement time $\rho \doteq \tau_{He}/\tau_E$, with a permissible operational value of $\rho \leqslant 7-15$.[22] This confinement time ratio is usually determined by the χ/D ratio. By looking again at Fig. 8 we can estimate a ratio $\chi/D \approx 2.5-3$ for GYRO and $\chi/D \approx 1.7$ for GLF23. Both estimates are essentially independent of dilution and give a reasonable estimate for our particular radial location. In reality, a detailed answer to the problem of helium ash removal will require a global simulation, follow-

ing the dynamics from core to edge. Our results here show that GLF23 could be well suited for such an efficient global study of this problem.

2. Outward impurity peaking

For negative $1/L_{nHe}$ (same figures) we discover a somewhat more interesting result: while the helium impurity ions experience a slightly improved confinement with increased f_{He} (this improvement is overestimated by GLF23), the bulk deuterium ions experience a degradation of confinement. In particular, at the critical value $f_{He} \simeq 0.07$ the deuterium goes from being pinched to flowing toward the plasma edge, but helium is flowing inward while the electrons are still pinched. This behavior has been previously noted; that is, whenever two ion species peak in different radial regions, the plasma is more unstable.[23] The physical mechanisms behind this phenomenon will be discussed in Sec. VIII. We remark that GLF23 captures this behavior quite accurately. A similar picture is observed for the energy confinement. For this particular regime, the agreement with GYRO is very good up to $f_{He} \simeq 0.1$ and fairly good beyond, except for the χ_{eff} calculation when $1/L_{nHe} = -1$.

3. The dilution model

Figure 9 looks at the variation of energy transport with dilution as obtained from both GYRO and GLF23. For the case of a negative impurity density gradient, as seen in Fig. 9(a), the dilution model applied to GYRO is in poor agreement with the fully kinetic model of impurities. In the opposite case, shown in Fig. 9(b), fair agreement is obtained for small values of dilution ($f_{He} < 0.05$), although for larger values a dramatic loss of accuracy is observed. Thus, when using GYRO, one should either treat impurities kinetically, or ignore them altogether. This is particularly true for the case of positive $1/L_{nHe}$ where impurities have a very weak effect on χ_{eff}/χ_{GBD} (i.e., small differences when compared to the pure plasma case) in the range 0.05–0.20. Figure 9(c) shows the equivalent results for GLF23. Surprisingly, we find that the dilution model gives rise to a result that is closer to the full dynamics than the pure plasma limit. This is apparently the result of the assumption in GLF23 of a similar ITG-type trial function for all values of f_{He}. In GYRO, however, no such assumption is made, and a nonphysical electron-direction mode is found when $f_{He} \geqslant 0.2$. This is the cause of the rapid accuracy loss of the GYRO dilution model. Separate GLF23 studies show the dilution model to behave similarly for deuterium-carbon plasmas—although with slightly lower accuracy than for deuterium-helium plasmas.

4. The lumped-mass approximation

Our study with this model was less exhaustive than for the dilution model. Only one case was considered ($f_{He}=0.3$, as shown by a triangle in Fig. 9), giving a DHe "atom" of mass $M=2.6$ and charge $Z=1.3$. This approximation is better than the dilution model, as would be expected for larger impurity fractions. Importantly, neither model can capture
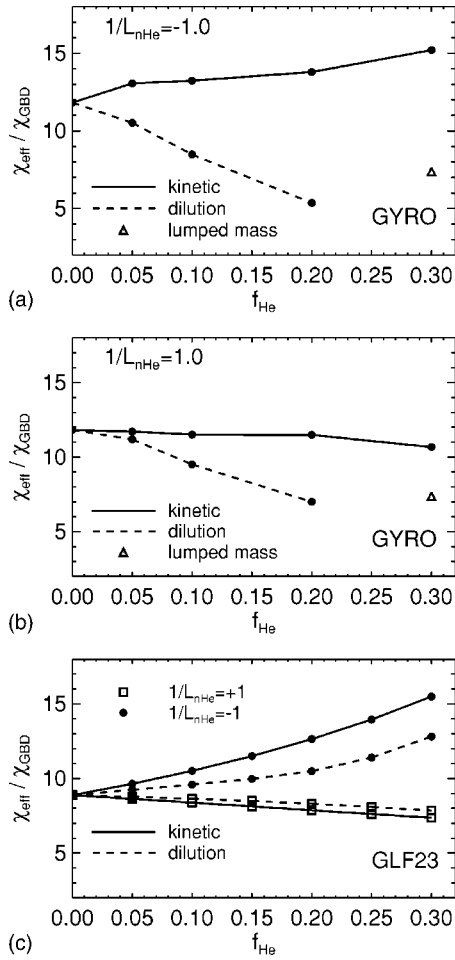
FIG. 9. f_{He} scans for $1/L_{nHe}=\pm1$, comparing the dilution model with full kinetic dynamics, for both GYRO and GLF23. Plot (a) shows GYRO runs at $1/L_{nHe}=-1$ while plot (b) shows GYRO runs at $1/L_{nHe}=1$. In both cases the lumped-mass approximation is included (triangle at $f_{He}=0.3$). Plot (c) shows the equivalent GLF23 calculations for $1/L_{nHe}=\pm1$ for both full dynamics and the dilution model.

the energy confinement degradation for $1/L_{nHe}<0$. Once again, it seems more sensible to approximate an impure plasma with its pure counterpart.

VII. PARTICLE TRANSPORT IN D-T PLASMAS

It is of interest to determine the particle and energy flux asymmetry in the case of a mixed deuterium-tritium plasma,

but before discussing such a problem it is useful to make some comments about *intrinsic* mass scaling. For ions of arbitrary mass m_i, the intrinsic mass scaling of frequency and diffusivity can be deduced:

$$\text{frequency} \rightarrowtail \frac{c_s}{a} \propto \frac{1}{m_i^{1/2}}, \quad \text{diffusivity} \rightarrowtail \chi_{GB} \propto m_i^{1/2}. \quad (8)$$

Strictly speaking, these scalings will be exactly obtained in the flux-tube (local) limit, such that the there is a single ion species, and the electron mass is removed from the problem—as in the adiabatic electron model. This means that if one simulates a pure-D plasma with adiabatic electrons and obtains $\chi_D = C\chi_{GBD}$, then the transport in other plasmas can be obtained by scaling arguments alone: $\chi = \sqrt{A/2}C\chi_{GBD}$, where A is the isotope atomic mass. Finite electron mass, as treated in this paper, will give rise to a relatively small breaking of these scaling rules through the nonadiabatic part of the electron response. This effect is evident from Table III, where we have summarized the results from a sequence of nonlinear GYRO simulations. Looking at the pure D, DT (fictitious species), and T energy diffusivities χ, we see that the ratios (1, 1.08, 1.21) deviate little from the expected $\sqrt{A/2}$ ratios (1, 1.11, 1.22).

The full nonlinear runs with kinetic electrons, as shown in Fig. 10, uncover two curious and potentially important results. First, in Fig. 10(a), we see that the deuterium energy diffusivity in the D-T simulation is actually enhanced slightly from that in the pure-plasma simulation. Second, in Fig. 10(b), we see that the tritium ions are more strongly pinched than either the deuterium ions in the D-T simulation or the deuterium ions in the pure-D simulations. We emphasize that for the D-T simulation, tritium is considered as the impurity, and so the normalization is with respect to χ_{GBD}—the gyro-Bohm diffusivity of deuterium. Although the differences in χ in Fig. 10(a) are small and at the limit of significance, we have verified that trends are preserved as the simulation resolution is changed.

An important potential implication of the stronger tritium pinch is that the resulting offset in particle flow for the two components imply that an initial 50-50 D-T mix in the plasma core will move toward a relatively higher fraction of tritium. The physical mechanism for this effect will be discussed in the following section. A curiosity of these results is apparent in the tritium energy transport, $\chi_T/\chi_{GBD}=11.73$, in

TABLE III. Summary of deuterium-tritium plasma study. All quantities already normalized to χ_{GBD} (deuterium gyro-Bohm diffusivity). The D simulation is the base Standard Case. The collisional D+T simulation has a relatively small collision frequency: $\nu_e=0.01$. Note that the identical value 11.73 in two separate cases is not a typo.

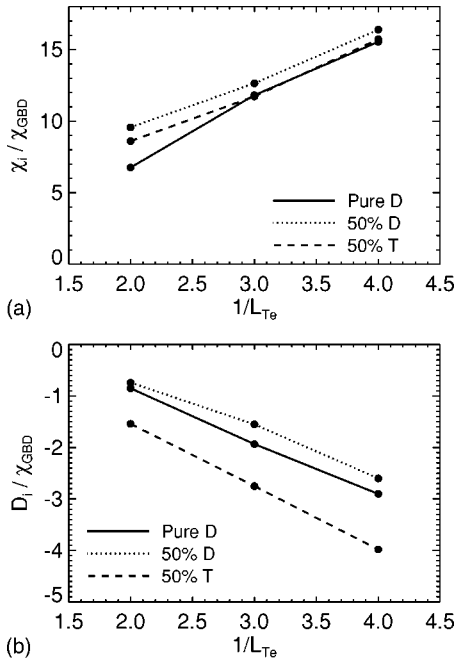| Simulation	χ_D	χ_{DT}	χ_T	D_D	D_{DT}	D_T
D	11.82	$\cdots$	$\cdots$	−1.93	$\cdots$	$\cdots$
Hybrid DT	$\cdots$	12.84	$\cdots$	$\cdots$	−2.19	$\cdots$
T	$\cdots$	$\cdots$	14.40	$\cdots$	$\cdots$	−2.49
D+T	12.65	$\cdots$	11.73	−1.55	$\cdots$	−2.75
Collisional D+T	12.47	$\cdots$	11.73	0.846	$\cdots$	0.128
Adiabatic D+T	4.023	$\cdots$	3.585	0.202	$\cdots$	−0.202

FIG. 10. Comparison of D-T transport coefficients with those from a pure-D plasma (solid curves). In the two-component DT simulation, we obtain separate transport coefficients for deuterium (dotted curve) and tritium (dashed curve). Plot (a) compares χ while plot (b) compares D. Recall that the normalization χ_{GBD} is computed with respect to pure deuterium.

a 50-50 plasma. This is about a 20% decrease from χ_T/χ_{GBD} as measured in a pure tritium simulation. However, there is a counterbalancing increase (although smaller in magnitude) in χ_D/χ_{GBD} from that measured in a pure deuterium simulation.

The addition of electron-ion collisions to the problem reduces the overall particle pinch strength but preserves the deuterium-tritium asymmetry. This is illustrated in Fig. 11, where a scan over $\eta_e = L_{ne}/L_{Te}$ shows that collisions shift the point of zero particle flow (the pinch null) to higher η_e.

VIII. ANALYSIS

Although a theoretical analysis using the full nonlinear GK equation is evidently impossible, we believe that linear and quasilinear analyses can shed some light on the phenom-
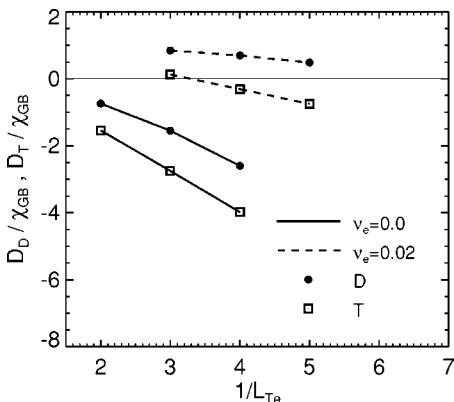
FIG. 11. Comparison of collisionless and collisional DT simulations for different values of $1/L_{Te}$. As usual the density gradient is fixed ($L_{ne}=1$) and the electron and ion temperature gradients are equal ($L_{Te}=L_{TD}$).

ena described in preceding sections. In particular, we are interested in understanding the helium pinch formation, the effect of impurity density gradient and dilution on energy confinement χ_{eff}, and the asymmetric flow of deuterium and tritium in a 50-50 mixture.

A. General theory

For all the calculations we begin from the linear GK equation. As always the unit of length is taken to be a, the unit of time is a/c_s and the unit of velocity is c_s.

$$\mu_\sigma \frac{v_\parallel}{qR} \frac{\partial g_\sigma}{\partial \theta} + (\omega + \omega_{d\sigma})g_\sigma$$

$$= n_\sigma(z_\sigma \omega + \omega_{*\sigma})J_0\left(\frac{bv_\perp}{z_\sigma \mu_\sigma}\right)\phi F_M. \tag{9}$$

In Eq. (9), g_σ is the nonadiabatic part of the perturbed gyro-center distribution function, n_σ is the ion density, ϕ is the normalized electrostatic potential ($\phi \doteq e\phi^p/T_e$, where ϕ^p is the physical potential), $\mu_\sigma \doteq \sqrt{m_1/m_\sigma}$ is the mass-ratio relative to the main ion, and $b \doteq k_\theta \rho_s \sqrt{1+s^2\theta^2}$ is the finite-Larmor-ratio (FLR) parameter. The velocity-dependent drifts are

$$\omega_{*\sigma} \doteq k_\theta \rho_s \left[\frac{1}{L_{n\sigma}} + \left(\frac{v_\perp^2 + v_\parallel^2 - 3}{2}\right)\frac{1}{L_T}\right], \tag{10}$$

$$\omega_{d\sigma} \doteq \frac{2k_\theta \rho_s}{z_\sigma R}\left(\frac{v_\perp^2}{4} + \frac{v_\parallel^2}{2}\right)(\cos\theta + s\theta\sin\theta). \tag{11}$$

Using the conventional $i\delta$ model for electrons, the Poisson (i.e., quasineutrality) equation for two ion species is

$$(1 - i\delta)n_e\phi = \sum_{\sigma=1,2} z_\sigma\left[z_\sigma f_\sigma + \int d^3v J_0\left(\frac{bv_\perp}{z_\sigma \mu_\sigma}\right)g_\sigma\right] \tag{12}$$

$$\doteq \sum_{\sigma=1,2} R_\sigma(\omega)n_e\phi. \tag{13}$$

Above, $f_\sigma \doteq z_\sigma n_\sigma/n_e$ is the charge factor such that $f_1+f_2=1$. Also, we have introduced a dimensionless linear response function for the ions R_σ. Note that the $i\delta$ model assumes electrons which are primarily adiabatic with an added, weak nonadiabatic correction δ to induce electron particle flow. Specifically, finite $\delta>0$ generates an outward electron flow and tend to destabilize electron directed drift waves. In the opposite case, $\delta<0$ generates an inward flow that tend to stabilize electron directed drift waves. The quasilinear particle fluxes at a given $k_\theta \rho_s$ are written as functions of the R_σ according to

$$\Gamma_\sigma = \text{Re}[ik_\theta \rho_s|\phi|^2 R_\sigma(\omega)n_e]. \tag{14}$$

In the quasilinear approximation, we take ω to be the complex linear mode frequency which is the solution of the eigenmode equation resulting from Eq. (13). There are various approximate methods for solution of the linear GK equations. For ions, the analysis is greatly simplified by ignoring particle trapping. This approximation, which is equivalent to working in the limit $r/R \ll 0$, is acceptable for realistic pa-

rameters and does not significantly alter the effects we are studying. We also ignore the parallel dynamics ($k_\parallel c_s/\omega \to 0$) entirely while exactly retaining the curvature drift resonance. This limit has been examined previously for the case of a pure plasma[24,25] and will be justified in a subsequent section. Under the indicated assumptions, the response functions can be written as

$$R_\sigma = -z_\sigma f_\sigma + \frac{f_\sigma}{\sqrt{2\pi}} \int_{-\infty}^{\infty} dv_\parallel e^{-v_\parallel^2/2} \int_0^{\infty} v_\perp dv_\perp e^{-v_\perp^2/2}$$

$$\times J_0^2\left(\frac{k_\theta \rho_s v_\perp}{z_\sigma \mu_\sigma}\right) \frac{z_\sigma \omega + \omega_{*\sigma}}{\omega + \omega_{d\sigma}}. \tag{15}$$

In Eq. (15), θ-dependent functions such as $\omega_{d\sigma}$ have been evaluated at $\theta = 0$. In terms of the response functions, the eigenvalue equation becomes

$$-(1 + i\delta) + R_1(\omega) + R_2(\omega) = 0. \tag{16}$$

The double integrals in Eq. (15) are straightforward to evaluate numerically, and the eigenvalue problem defined by Eq. (16) can be thus solved by application of a root finder. The integral form of the dispersion relation is in fact a very good linear ITG model. To obtain a purely analytic solution, we can expand the integrand in Eq. (15) through orders $O(k_\theta \rho_s)$, $O(\omega_d/\omega)$, $O(\omega_d/\omega \times k_\theta \rho_s)$ to yield the response functions

$$R_\sigma = f_\sigma \left\{ \frac{\omega_{*n\sigma}}{\omega} - \frac{\omega_d}{\omega}\left(1 + \frac{\omega_{*p\sigma}}{z_\sigma \omega}\right) - \frac{(k_\theta \rho_s)^2}{\mu_\sigma^2}\left[\left(1 + \frac{\omega_{*p\sigma}}{\omega}\right) \right.\right.$$

$$\left.\left. - \frac{3}{2}\frac{\omega_d}{\omega}\left(1 + \frac{\omega_{*p\sigma} + \omega_{*T}}{z_\sigma \omega}\right)\right]\right\}, \tag{17}$$

where $\omega_{*n\sigma} = k_\theta \rho_s/L_{n\sigma}$, $\omega_{*T} = k_\theta \rho_s/L_T$, $\omega_{*p\sigma} = \omega_{*n\sigma} + \omega_{*T}$, and $\omega_d = k_\theta \rho_s(2/R)$. Note that ω_d, as defined here, has no species dependence. Despite the seeming complexity of the response functions, the resulting eigenvalue equation is a simple quadratic in ω. We refer to Eq. (17) as the *nonresonant expansion* because it neglects the physical effects of the drift resonance.

Finally, by writing $\omega = \omega_R + i\gamma$ and using Eqs. (14) and (17), the explicit form of the quasilinear particle fluxes at a given $k_\theta \rho_s$ is given by

$$\Gamma_\sigma = k_\theta \rho_s |\phi|^2 n_e \frac{\gamma f_\sigma}{|\omega|^2}\left\{\omega_{*n\sigma} - \omega_d\left(1 + \frac{2\omega_R \omega_{*p\sigma}}{z_\sigma |\omega|^2}\right) - \frac{(k_\theta \rho_s)^2}{\mu_\sigma^2}\right.$$

$$\left. \times \left[\omega_{*p\sigma} - \frac{3}{2}\omega_d\left(1 + \frac{2\omega_R(\omega_{*p\sigma} + \omega_{*T})}{z_\sigma |\omega|^2}\right)\right]\right\}. \tag{18}$$

B. Helium pinch formation

We focus on the case $1/L_{n\text{He}} > 0$, which is the more relevant for helium ash transport. In the limit of small helium fraction, it is simple to compute the helium flow in the long-wavelength limit. We are specifically interested in computing the null point of helium flow, and so are interested in the zero of

$$\Gamma_\text{He} \propto -\text{Im}\, R_\text{He} \sim -f_\text{He}\, \text{Im}\left(\frac{\omega_{*n\text{He}} - \omega_d}{\omega} - \frac{\omega_d \omega_{*p\text{He}}}{2\omega^2}\right)$$

$$+ O(k_\theta \rho_s)^2. \tag{19}$$

We will work in the limit of small δ, f_He, and $k_\theta \rho_s$. To determine the eigenmode frequency it is sufficiently accurate to solve

$$-(1 - i\delta) + \frac{\omega_{*n\text{D}} - \omega_d}{\omega} - \frac{\omega_{*p\text{D}} \omega_d}{\omega^2} = 0. \tag{20}$$

This expression can be use to write $\text{Im}(1/\omega^2)$ in terms of $\text{Im}(1/\omega)$, yielding a simple equation for the flow null

$$-\text{Im}\, R_\text{He} = f_\text{He}\left[(\omega_{*n\text{He}} - \omega_d) - \frac{\omega_{*p\text{He}}}{2\omega_{*p\text{D}}}(\omega_{*n\text{D}} - \omega_d)\right]\frac{\gamma}{|\omega|^2}$$

$$+ f_\text{He}\frac{\delta}{2}\frac{\omega_{*p\text{He}}}{\omega_{*p\text{D}}} = 0, \tag{21}$$

where $\gamma/|\omega|^2 \sim 1/(\omega_{*p\text{D}} \omega_d)^{1/2}$. For the Standard Case parameters, Eq. (21) predicts that the flow null will occur at $L_{n\text{He}}/L_{ne} = 0.84$ (the zero of the term in square brackets) in the adiabatic electron limit ($\delta = 0$). To make a comparison with GYRO results, it is useful to perform simulations both with and without adiabatic electrons. This elucidates the particular effect that electron dynamics has on the helium transport, as can be seen in Fig. 7. For kinetic electrons (and $f_\text{He} = 0.1$) the GYRO flow null occurs at $L_{n\text{He}}/L_{ne} = 1.4$, whereas for adiabatic electrons it occurs at $L_{n\text{He}}/L_{ne} = 2.0$. To understand the source of the discrepancy between the GYRO and analytic values, we solved Eqs. (15) and (16) numerically. These more accurate equations predict that the flow null is located at $L_{n\text{He}}/L_{ne} = 2.22$ in very good agreement with the adiabatic electron simulations. This lead us to conclude that the discrepancy between the simulation value, $L_{n\text{He}}/L_{ne} = 2.0$, and our analytical prediction, $L_{n\text{He}}/L_{ne} = 0.84$, is due to the omission of curvature drift resonance effects in Eq. (17). Nevertheless, from Eq. (21), we can still understand the pinch mechanism for which toroidal curvature plays the main role. The term $(\omega_{*n\text{He}} - \omega_d)$ in Eq. (21) represents the interplay of curvature and helium drift physics, with curvature driving the pinch. The second term is the back reaction of the analogous curvature-induced deuterium pinch. That is, as more deuterium flows inwards, some helium must flow out to compensate in order to maintain ambipolarity. Finally, we remark that the nonresonant theory also predicts a helium pinch for $L_{n\text{He}}/L_{ne} > 0.84$, and outward flow for $L_{n\text{He}}/L_{ne} < 0.84$, in qualitative agreement with both kinetic and adiabatic electrons simulations.

C. Density gradient and dilution effects on energy confinement

The purpose of this analysis is to understand the effect of $1/L_{n\text{He}}$ and f_He on χ_{eff}. Scans over a range of f_He for two values of $1/L_{n\text{He}}$ are reproduced in Fig. 9. From this figure, a puzzle emerges: why do inwardly peaked impurities ($1/L_{n\text{He}} = 1$) tend to stabilize the plasma while the opposite effect is found for outwardly peaked impurities ($1/L_{n\text{He}} = -1$)? After all, as seen from Eq. (4), an increase in f_He

TABLE IV. Physical realism of linear, adiabatic-electron calculations summarized in Table V. "Trapping" refers to ion trapping, "parallel motion" to treating $\partial/\partial\theta$ and the θ dependence of the drifts exactly, "FLR" to full inclusion of finite-Larmor-radius effects, and "drift resonance" to a nonperturbative treatment of the curvature drift resonance. RF denotes the "root finder" solution of Eqs. (15) and (16), while "analytic" refers to Eqs. (22) and (23).

Model	(1) GYRO	(2) GYRO	(3) GYRO	(4) GYRO	(5) RF	(6) Analytic
Trapping	×					
Parallel motion	×	×				
FLR	×	×	×			
Drift resonance	×	×	×	×	×	

decreases L_{ni} and consequently η_i when $1/L_T$ is kept fixed. Therefore, based on ITG physics alone, increasing f_{He} should stabilize the plasma in contradiction with our nonlinear results.

In the context of numerical simulations, this issue has been considered previously[7] where a strong coupling between the ITG and impurities is found to be responsible for this behavior, although no details of this coupling is given. To properly diagnose the situation, in what follows, we will compare results from a simple linear eigenvalue equation to GYRO linear calculations. Using the nonresonant expansion, Eq. (17), we solve Eq. (16) to find growth rates

$$\gamma_\pm = \sqrt{\gamma_{pure}^2 - \frac{f_{He}\omega_d}{2}(\omega_{*T} \pm |\omega_{*nHe}|)}, \tag{22}$$

where

$$\gamma_{pure}^2 = \frac{4\omega_d(\omega_{*ne} + \omega_{*T}) - (\omega_{*ne} - \omega_d)^2}{4} \tag{23}$$

is the growth rate when $f_{He}=0$. Here, $\omega_{*ne}=k_\theta\rho_s(1/L_{ne})$ and $\omega_d=k_\theta\rho_s(2/R)$. In $\gamma_\pm$ the plus sign refers to the $1/L_{nHe}>0$ case while the minus sign refers to $1/L_{nHe}<0$. As before $O(k_\theta\rho_s)^2$ corrections are neglected. The last formulas imply that $\gamma_- > \gamma_+$ for a given value of dilution according to what is found in Ref. 23. However, these analytic estimates predict $\gamma_{pure} > \gamma_-$ and $\gamma_{pure} > \gamma_+$. Although the later is true, the former is in contradiction with linear[7] and nonlinear (Fig. 9) simulations where $\gamma_{pure} < \gamma_-$. To resolve this discrepancy, we must turn to a more accurate calculation of growth rates.

Table IV describes in detail the assumptions which define each of six separate linear calculations. Here, (1) is the most realistic set of assumptions and (6) the least realistic. Table V shows the normalized growth rates, for each of the six cases described in Table IV for $1/L_{nHe}=\pm1$. In Table V,

the results for $1/L_{nHe}=1$ show agreement in trend with nonlinear simulations (that is, increasing f_{He} stabilizes the plasma). It also shows that trapping plays a minor role [compare (1) and (2)] while $v_\parallel$ has no effect [compare (2) and (3)] justifying the assumptions made for our analytical calculations. For the case of finite-Larmor-radius (FLR) effects we see a stronger variation, but as mentioned before the qualitative behavior is not modified. For the opposite case ($1/L_{nHe}=-1$) a more interesting behavior is observed. When all physics effects are included [see (1)] we can see the trend predicted in Fig. 9 where outwardly peaked impurities tend to destabilize the plasma when compared to the pure plasma case. However, as physical effects are removed, the destabilizing trend is almost eliminated for the GYRO simulations [cases (2)–(4)] and the root finder (RF) code [see (5); solution of Eqs. (15) and (16)]. It is only the analytic result which shows a reversal in the trend [see (6); Eqs. (22)] indicating that the effect observed in Fig. 9 is mainly caused by the drift resonance [see Eq. (15)]. Moreover, by comparing the last column of Table V, we see that the direction of the density gradient $1/L_{nHe}$ does not seem to play as large a role in the instability formation as initially thought. Finally it is worth mentioning that parallel motion and FLR effects play a very small role and therefore their exclusion is justified.

The main conclusion from these results is that although impurities play some direct role, the behavior observed is mostly the result of all the physical mechanisms involved in the problem such as particle trapping, parallel motion, FLR, and more important the drift resonance.

D. D-T flow separation

Perhaps the most curious nonlinear simulation result is the observation of an asymmetric flow of deuterium and tritium in a 50-50 mixture. Upon discovering this asymmetry,

TABLE V. Summary of growth rate shift, γ/γ_0, for $1/L_{nHe}=\pm1$ and $f_{He}=0.1,0.3$ for each of the six models outlined in Table IV. Here, γ_0 refers to the growth rate at $f_{He}=0$ for a given $1/L_{nHe}$ and model.

$1/L_{nHe}$	f_{He}	(1)	(2)	(3)	(4)	(5)	(6)
1	0.1	0.972	0.970	0.970	0.960	0.967	0.890
1	0.3	0.938	0.930	0.930	0.880	0.911	0.611
−1	0.1	1.028	1.0	1.0	1.001	1.008	0.947
−1	0.3	1.355	1.085	1.085	1.040	1.040	0.829

we then computed quasilinear flow estimates using linear GYRO simulations. We found that the quasilinear estimates also robustly exhibited the D-T flow asymmetry of the non-linear simulations—predicting that the tritium flow is directed inward and the deuterium flow of equal magnitude outward. This motivated us to search for a simple analytic expression which could give some physical insight into the symmetry breaking. Setting $z_D = z_T = 1$, and $f_D = f_T = 1/2$, and noting that that response functions have the form

$$R_D = A(\omega) + B(\omega), \quad R_T = A(\omega) + \frac{1}{\mu_T^2} B(\omega), \tag{24}$$

with $\mu_T^2 = 2/3$, we can write the eigenvalue equation as

$$-(1 - i\delta) + 2A(\omega) + \left(1 + \frac{1}{\mu_T^2}\right) B(\omega) = 0, \tag{25}$$

where

$$A(\omega) = \frac{\omega_{*n}}{2\omega} - \frac{\omega_d}{2\omega}\left(1 + \frac{\omega_{*p}}{\omega}\right), \tag{26}$$

$$B(\omega) = -\frac{(k_\theta \rho_s)^2}{2}\left[\left(1 + \frac{\omega_{*p}}{\omega}\right) - \frac{3}{2}\frac{\omega_d}{\omega}\left(1 + \frac{\omega_{*p} + \omega_{*T}}{\omega}\right)\right]. \tag{27}$$

By demanding that the eigenvalue equation be satisfied, it is easy to show that the imaginary part of the response functions become

$$\mathrm{Im}\, R_D = -\frac{1}{2}\left(\frac{1}{\mu_T^2} - 1\right) B(\omega) - \frac{\delta}{2},$$

$$\mathrm{Im}\, R_T = \frac{1}{2}\left(\frac{1}{\mu_T^2} - 1\right) B(\omega) - \frac{\delta}{2}. \tag{28}$$

In the regime $\omega_{*p} \gg \omega_d \gg (k_\theta \rho_s)^2 \omega_{*p}$, we can compute a crude but illustrative expression for the explicit quasilinear particle flow, as defined by Eq. (14), at a given value of $k_\theta \rho_s$:

$$\Gamma_D = n_e (k_\theta \rho_s)|\phi|^2(-\mathrm{Im}\, R_D)$$
$$= +\frac{n_e}{8}(k_\theta \rho_s)^3|\phi|^2\sqrt{\frac{1}{2}\left(\frac{R}{L_n} + \frac{R}{L_T}\right)} + \frac{n_e}{2}\delta(k_\theta \rho_s)|\phi|^2, \tag{29}$$

$$\Gamma_T = n_e (k_\theta \rho_s)|\phi|^2(-\mathrm{Im}\, R_T)$$
$$= -\frac{n_e}{8}(k_\theta \rho_s)^3|\phi|^2\sqrt{\frac{1}{2}\left(\frac{R}{L_n} + \frac{R}{L_T}\right)} + \frac{n_e}{2}\delta(k_\theta \rho_s)|\phi|^2. \tag{30}$$

The quasilinear result is quite robust, and indicates that in the (adiabatic) limit $\delta = 0$, for any form of the potential (i.e., independent of any mixing-length or similar assumptions) the tritium will flow inward and the deuterium outward at every value of $k_\theta \rho_s$. Note that the total transport coefficient is obtained by summation over the toroidal mode number n in $k_\theta \rho_s = (nq/r)\rho_s$. At finite $\delta > 0$, we observe that the added effect of electron dynamics is to symmetrically drive an outward flow of both species whereas in the opposite case (δ

< 0) an inward flow is driven. This shows that, within the accuracy of the $i\delta$ model, the particle flow asymmetry is purely an ion effect.

However, the DT flow separation effect discussed in this section is simply the result of having $f_D = f_T = 1/2$ and $1/L_{nD} = 1/L_{nT} = 1$. This in turn makes $A(\omega)$ the same for both species and consequently $B(\omega)/\mu_T^2$, which is $O(k_\theta \rho_s)^2$, the only source of asymmetry. In the case of a real fusion plasma where the previous equalities may not be satisfied, $A(\omega)$ which is $O(1)$ and different for deuterium and tritium, will dominate the dynamics of the particle fluxes.

In order to look at this effect in more detail we write $\Gamma_D = \Gamma_e/2 + \Delta$ and $\Gamma_T = \Gamma_e/2 - \Delta$. For the sake of clarity we consider two cases. The first case looks at f_T variations keeping the density gradients fixed and equal ($1/L_{nD} = 1/L_{nT} = 1$), whereas in the second case we consider $1/L_{nT}$ variations with fixed $f_T = 1/2$. In both cases electron dynamics is not included ($\Gamma_e = 0$). To complement this analysis we use again the RF code [solution of Eqs. (15) and (16)] used in the preceding section. For the first case we find that $\Delta \propto f_T$ as expected from ambipolarity constraints and no electron dynamics. In the second case we find a more interesting situation in which the particle flow is controlled by the density gradients of deuterium and tritium. For instance, when the density gradient of tritium is steepened enough, the deuterium flows inward while the tritium flows outward as opposed to the $1/L_{nD} = 1/L_{nT}$ case. This effect is reversed when the tritium density gradient is flattened enough. This comes from the fact that Eq. (4) is always enforced. The point of zero flow occurs at $1/L_{nT} = 1.0398$ which indicates that the DT 50-50 effect found is very subtle indeed and that the slightest deviation from equal density gradients can restore equal D and T flows.

E. On The accuracy of selected approximations

In attempting to construct an analytic theory of ITG modes which is reasonably accurate for typical tokamak parameters, one soon finds that many of the more popular approaches are rather problematic. Certain models, such as the ubiquitous *slab approximation* (which sets $\omega_d/\omega = 0$), may often be next to useless. A more sophisticated model which appears in the literature is derived by working to leading order in ω_d/ω, $k_\theta \rho_s$, and $k_\parallel c_s/\omega$ (the so-called fluid limit) to derive a soluble second-order differential equation for the eigenfrequency.[25–27] However, in this model, the neglect of resonant curvature drift effects leads to a rather serious error in the phase of the eigenfrequency and is thus a poor approximation for many purposes. For example, the eigenfrequency $\omega = \omega_R + i\gamma$ in the fluid limit tends to be almost purely growing, with $\omega_R \sim 0$. In reality, toroidal ITG modes for the Standard Case typically satisfy $|\omega_R| > |\gamma|$. This undesireable feature of the fluid limit is a consequence of the perturbative expansion in ω_d/ω. It turns out that for realistic parameters, it is better to ignore $O(k_\parallel c_s/\omega)$ terms completely (thus transforming the problem to an algebraic rather than a differential one) and instead focus on working to higher order (or in fact, nonperturbatively) in ω_d/ω.

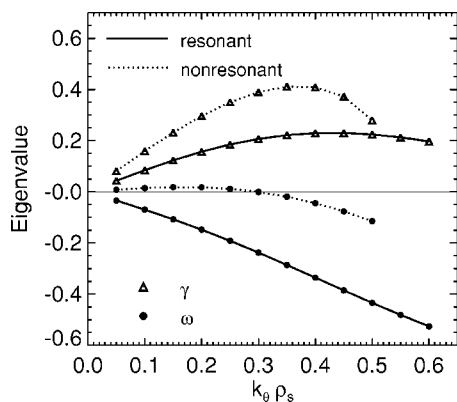By referring to Fig. 12, one can see clearly the difference

FIG. 12. Comparison of eigenfrequencies for theory including nonperturbative drift resonance (solid curves) with those from the nonresonant expansion (dotted curves). Standard Case parameters for a 50-50 D-T plasma are used.

between working to lowest order in ω_d/ω (nonresonant theory) and nonperturbatively in ω_d/ω (resonant theory) for a D-T plasma. As claimed, the nonresonant theory predicts an eigenfrequency which is almost pure imaginary, while the resonant theory correctly predicts that the mode rotates strongly in the ion direction. To more systematically describe the effects of each approximation, we consider five different calculations of the quasilinear deuterium flow of the preceding section. Figure 13(a) shows the exact value [GYRO (1)] compared with that obtained by neglecting trapping [GYRO (2)] and parallel motion [GYRO (3)] entirely. The salient
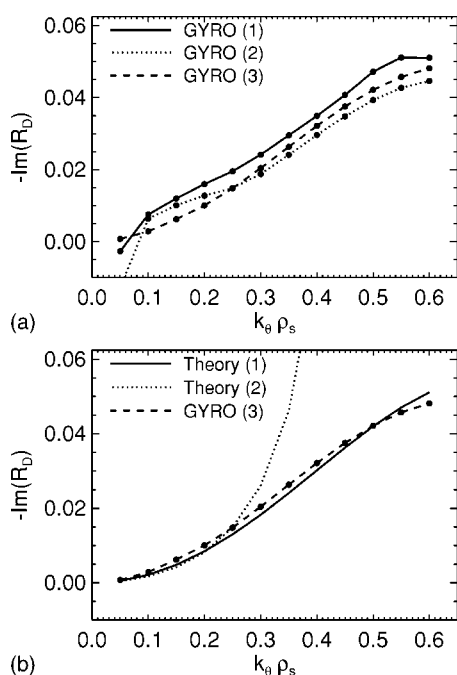

FIG. 13. Plot (a) compares three GYRO calculations of the quasilinear deuterium flow in a 50-50 D-T plasma for the Standard Case. GYRO (1) makes no approximation. GYRO (2) neglects particle trapping by setting r =0.05 [whereas GYRO (1) has r=0.5] and GYRO (3) ignores the parallel motion (ion-sound physics) altogether. Plot (b) compares the GYRO (3) simulation with the full local kinetic theory [theory (1), which uses Eq. (15)] and the long-wavelength local kinetic theory [theory (2), which uses the simpler Eq. (17)].

point is that parallel motion can be safely ignored. In Fig. 13(b), it is evident that the resonant integral theory [theory (1)] agrees extremely well with the GYRO calculation that neglects parallel motion [GYRO (3)]. This, we believe the resonant integral theory should be used in any case where an accurate but still tractable model is required. Surprisingly, Fig. 13(b) also shows that the nonresonant theory [theory (2)] gives a very good description of the quasilinear flow in the low-to-moderate $k_\theta\rho_s$ range. This lends some degree of confidence to the analytic results in Eqs. (29) and (30).

IX. CONCLUSIONS

The principal results of this investigation can be separated into three categories: *pure plasmas, plasmas with impurities*, and *isotope flow separation*.

In pure plasmas, the different pinch formation mechanisms were studied, indicating that the temperature gradient plays the dominant role. Electron collisions, on the other hand, generally oppose the production of a thermal pinch.

In plasmas with impurities, the effects of impurity density gradients and dilution were considered. For moderate values of the helium density gradient, a helium pinch can be created and is driven largely by finite toroidicity (curvature). Further, we found that the direction of the density gradient introduces substantial qualitative and quantitative changes to the plasma—for example, a plasma with impurities peaked in the core has better energy confinement than a plasma with impurities peaked at the edge. Finally, we examined the validity of different approximations to transport in multiple-species plasmas; specifically, the dilution model and lumped-mass approximation. It was found that it is best to approximate an impure plasma with the simplest alternative—a pure plasma—at least when both species are similar (such as for deuterium and helium). Perhaps the most commonly discussed impurity problem is that of a deuterium-carbon plasma, but we have focused on deuterium-helium plasmas because most experiments are done with helium and because the helium ash removal is an important problem for burning plasmas (Ref. 28, and references therein). For the nominal parameters studied in this paper, the deuterium core ions flow inward and the helium impurity ions flow outward.

Finally, reactor-relevant D-T plasmas were analyzed. Contrary to what is normally assumed, the turbulent flows of deuterium and tritium are not equal but show an asymmetry. Starting from an optimal 50-50 mixture, the asymmetry favors the buildup of tritium in the core. A quasilinear model shows that this asymmetry is caused by FLR effects. However, a small steepening of the tritium profile can restore equal flows of D and T.

[1] ITER Physics Basic Editors, Nucl. Fusion **39**, 2175 (1999).

[2] J. Candy and R. E. Waltz, J. Comput. Phys. **186**, 545 (2003).

[3] D. W. Ross and W. Dorland, Phys. Plasmas **9**, 5031 (2002).

[4] J. Candy and R. E. Waltz, Phys. Rev. Lett. **91**, 045001 (2003).

[5] D. R. Ernst, P. T. Bonoli, P. J. Catto, W. Dorland, C. L. Fiore, R. S. Granetz, M. Greenwald, A. E. Hubbard, M. Porkolab, M. H. Redi, J. E. Rice, K. Zhurovich, and Alcator C-Mod Group, Phys. Plasmas **11**, 2637 (2004).

[6] J. Q. Dong, W. Horton, and W. Dorland, Phys. Plasmas **1**, 3635 (1994).

[7] J. Q. Dong and W. Horton, Phys. Plasmas **2**, 3412 (1995).

[8] W. Dorland, F. Jenko, M. Kotschenreuther, and B. N. Rogers, Phys. Rev. Lett. **85**, 5579 (2000).

[9] M. Kotschenreuther, G. Rewoldt, and W. M. Tang, Comput. Phys. Commun. **88**, 128 (1995).

[10] R. E. Waltz, G. M. Staebler, W. Dorland, G. W. Hammett, M. Kotschenreuther, and J. A. Konings, Phys. Plasmas **4**, 2482 (1997).

[11] K. Hallatschek and W. Dorland, Bull. Am. Phys. Soc. **47**, 135 (2002).

[12] B. Coppi and C. Spight, Phys. Rev. Lett. **41**, 551 (1978).

[13] R. E. Waltz, W. Pfeiffer, and R. R. Dominguez, Nucl. Fusion **20**, 43 (1980).

[14] R. E. Waltz and R. R. Dominguez, Phys. Fluids B **1**, 1935 (1989).

[15] V. V. Yancov, JETP Lett. **60**, 171 (1994).

[16] M. B. Isichenko, A. V. Gruzinov, and P. H. Diamond, Phys. Rev. Lett. **74**, 4436 (1995).

[17] D. R. Baker and M. N. Rosenbluth, Phys. Plasmas **5**, 2936 (1998).

[18] D. R. Baker, Phys. Plasmas **11**, 992 (2004).

[19] X. Garbet, L. Garzotti, P. Mantica, H. Nordman, M. Valovic, H. Weisen, and C. Angioni, Phys. Rev. Lett. **91**, 035001 (2001).

[20] C. Angioni, A. G. Peeters, G. V. Pereverzev, F. Ryter, G. Tardini, and ASDEX Upgrade Team, Phys. Plasmas **10**, 3225 (2003).

[21] G. R. McKee, M. Murakami, J. A. Boedo, N. H. Brooks, K. H. Burrell, D. R. Ernst, R. J. Fonck, G. L. Jackson, M. Jakubowski, R. J. La Haye, A. M. Messiaen, J. Ongena, C. L. Rettig, B. W. Rice, C. Rost, G. M. Staebler, R. D. Sydora, D. M. Thomas, B. Unterberg, M. R. Wade, and W. P. West, Phys. Plasmas **7**, 1870 (2000).

[22] D. Reiter, G. H. Wolf, and H. Kever, Nucl. Fusion **30**, 2141 (1990).

[23] B. Coppi, H. P. Furth, M. N. Rosenbluth, and R. Z. Sagdeev, Phys. Rev. Lett. **17**, 377 (1966).

[24] P. W. Terry, W. Anderson, and W. Horton, Nucl. Fusion **22**, 487 (1982).

[25] F. Romanelli, Phys. Fluids B **1**, 1018 (1989).

[26] R. J. Hastie, K. W. Hesketh, and J. B. Taylor, Nucl. Fusion **19**, 1223 (1979).

[27] C. Z. Cheng and K. T. Tsang, Nucl. Fusion **21**, 643 (1981).

[28] M. R. Wade, D. L. Hillis, J. T. Hogan, R. Maingi, M. M. Menon, M. A. Mahdavi, W. P. West, K. H. Burrell, P. Gohil, R. J. Groebner, R.-M. Hong, D. H. Kellman, J. C. Phillips, R. P. Seraydarian, the DIII-D Team, and D. F. Finkenthal, Phys. Plasmas **2**, 2357 (1995).